Bowtie plasmonic quantum cascade laser antenna

**Nanfang Yu[1], Ertugrul Cubukcu[1], Laurent Diehl[1], David Bour[2,a],
Scott Corzine[2,b], Jintian Zhu[2], Gloria Höfler[2,c], Kenneth B. Crozier[1], and
Federico Capasso[1]***

[1]*School of Engineering and Applied Sciences, Harvard University Cambridge, Massachusetts 02138, USA*
[2]*Agilent Laboratories, 3500 Deer Creek Road, Palo Alto, California 94304, USA*
Current affiliations:
[a]*Bridgelux Inc, 1225 Bordeaux Dr, Sunnyvale, California 94089, USA*
[b]*Infinera HQ, 169 Java Dr, Sunnyvale, California 94089, USA*
[c]*Argos Tech LLC, 3671 Enochs St, Santa Clara, California 95051, USA*
Corresponding author: capasso@seas.harvard.edu

Abstract: We report a bowtie plasmonic quantum cascade laser antenna that can confine coherent mid-infrared radiation well below the diffraction limit. The antenna is fabricated on the facet of a mid-infrared quantum cascade laser and consists of a pair of gold fan-like segments, whose narrow ends are separated by a nanometric gap. Compared with a nano-rod antenna composed of a pair of nano-rods, the bowtie antenna efficiently suppresses the field enhancement at the outer ends of the structure, making it more suitable for spatially-resolved high-resolution chemical and biological imaging and spectroscopy. The antenna near field is characterized by an apertureless near-field scanning optical microscope; field confinement as small as 130 nm is demonstrated at a wavelength of 7.0 μm.

References and links

1. F. Zenhausern, M. P. O'Boyle, and H. K. Wickramasinghe, "Apertureless near-field optical microscope," Appl. Phys. Lett. **65**, 1623-1625 (1994).
2. A. Lahrech, R. Bachelot, P. Gleyzes, and A. C. Boccara, "Infrared-reflection-mode near-field microscopy using an apertureless probe with a resolution of λ/600," Opt. Lett. **21**, 1315-1317 (1996).
3. J. Jersch, F. Demming, L. J. Hildenhagen, and K. Dickmann, "Field enhancement of optical radiation in the nearfield of scanning probe microscope tips," Appl. Phys. A. **66**, 29-34 (1998).
4. N. Calander and M. Willander, "Theory of surface-plasmon resonance optical-field enhancement at prolate spheroids," J. Appl. Phys. **92**, 4787-4884 (2002).
5. E. Cubukcu, E. A. Kort, K. B. Crozier, and F. Capasso, "Plasmonic laser antenna," Appl. Phys. Lett. **89**, 093120 (2006).
6. N. Yu, E. Cubukcu, L. Diehl, K. B. Crozier, and F. Capasso, "Plasmonic quantum cascade laser antenna," in *CLEO/QELS Conference* 2007 (American Physical Society, IEEE Lasers and Electro-Optics Society, and Optical Society of America, 2007), paper JMA6.
7. N. Yu, E. Cubukcu, L. Diehl, M. Belkin, K. B. Crozier, D. Bour, S. Corzine, G. Höfler, and F. Capasso, "Plasmonic quantum cascade laser antenna," Appl. Phys. Lett. (unpublished).
8. T. Taubner, R. Hillenbrand, and F. Keilmann, "Nanoscale polymer recognition by spectral signature in scattering infrared near-field microscopy," Appl. Phys. Lett. **85**, 5064-5066 (2004).
9. M. B. Raschke, L. Molina, T. Elsaesser, D. H. Kim, W. Knoll, and K. Hinrichs, "Apertureless near-field vibrational imaging of block-copolymer nanostructures with ultrahigh spatial resolution," ChemPhysChem **6**, 2197-2203 (2005).
10. M. Brehm, T. Taubner, R. Hillenbrand, and F. Keilmann, "Infrared spectroscopic mapping of single nanoparticles and viruses at nanoscale resolution," Nano Lett. **6**, 1307-1310 (2006).
11. K. B. Crozier, A. Sundaramurthy, G. S. Kino, and C. F. Quate, "Optical antennas: resonators for local field enhancement," J. Appl. Phys. **94**, 4632-4642 (2003).
12. R. W. P. King, H. R. Mimno, and A. H. Wing, *Transmission Lines, Antennas and Wave Guides* (McGraw-Hill Book Company, 1945), Sec. 29.

13. W. L. Stutzman, and G. A. Thiele, *Antenna Theory and Design* (John Wiley & Sons, Inc. 1981), Chap. 5.
14. F. Neubrech, T. Kolb, R. Lovrincic, G. Fahsold, A. Pucci, J. Aizpurua, T. W. Cornelius, M. E. Toimil-Molares, R. Neumann, and S. Karim, "Resonances of individual metal nanowires in the infrared," Appl. Phys. Lett. **89**, 253104 (2006).
15. J. Faist, F. Capasso, D. L. Sivco, C. Sirtori, A. L. Hutchinson, and A. Y. Cho, "Quantum cascade laser," Science **264**, 553-556 (1994).
16. F. Capasso, C. Gmachl, D. L. Sivco, and A. Y. Cho. Phys. Today. "Quantum cascade lasers," **55**, 34-40 (2002).
17. J. W. Cooper, *Spectroscopic Techniques for Organic Chemists* (John Wiley and Sons, Inc. 1980), Chap. 1.
18. L. Diehl, D. Bour, S. Corzine, J. Zhu, G. Höfler, M. Lončar, M. Troccoli, and F. Capasso, "High-power quantum cascade lasers grown by low-pressure metal organic vapor-phase epitaxy operating in continuous wave above 400 K," Appl. Phys. Lett. **88**, 201115 (2006).
19. A. A. Kosterev, and F. K. Tittel, "Chemical sensors based on quantum cascade lasers," IEEE J. Quantum Electron. **38**, 582-591 (2002).
20. B. Lendl, J. Frank, R. Schindler, A. Müller, M. Beck, and J. Faist, "Mid-infrared quantum cascade lasers for flow injection analysis," Anal. Chem. **72**, 1645-1648 (2000).
21. FDTD simulations were performed using a commercial software XFdtd (Remcom Inc.): http://www.remcom.com/
22. L. Novotny, "Effective wavelength scaling for optical antennas," Phys. Rev. Lett. **98**, 266802 (2007).
23. K. S. Kunz, and R. J. Luebbers, *the Finite Difference Time Domain Method for Electromagnetics* (CRC Press, 1993), Chap. 8.
24. E. D. Palik, *Handbook of Optical Constants* (Academic, 1985).
25. N. Yu, L. Diehl, E. Cubukcu, C. Pflügl, D. Bour, S. Corzine, J. Zhu, G. Höfler, K. B. Crozier, and F. Capasso, "Near-field imaging of quantum cascade laser transverse modes," Opt. Express (unpublished).
26. R. Hillenbrand, B. Knoll, and F. Keilmann, "Pure optical contrast in scattering-type scanning near-field microscopy," J. Microsc. **202**, 77-83 (2001).
27. B. Knoll, and F. Keilmann, "Enhanced dielectric contrast in scattering-type scanning near-field optical microscopy," Opt. Commun. **182**, 321-328 (2000).
28. M. Troccoli, S. Corzine, D. Bour, J. Zhu, O. Assayag, L. Diehl, B. G. Lee, G. Höfler, and F. Capasso, "Room temperature continuous-wave operation of quantum-cascade lasers grown by metal organic vapour phase epitaxy," Electron. Lett. **41**, 1059-1060 (2005).

1. Introduction

In a conventional apertureless near-field scanning optical microscope (a-NSOM), a spatially-confined optical spot at the end of a metallic scanning tip enables nanometric features in samples to be selectively illuminated, resulting in spatial resolution exceeding the diffraction limit [1, 2]. In such a passive system, an external light source and some intermediate optics are utilized to illuminate the scanning tip; the generation of localized surface plasmon waves as well as the "lightning-rod effect" create a subwavelength optical spot at the apex of the sharp tip [3, 4]. The system could be greatly simplified if the light source and the nanostructure, which confines the electric field to subwavelength dimensions, could be combined in an *active* device. Recently, some efforts have been made to realize such active devices in both the near-infrared (near-ir) and the mid-infrared (mid-ir) regions [5-7]. These devices, termed plasmonic laser antennas, were implemented by defining metallic nano-antennas on the facets of near-ir commercial laser diodes and mid-ir quantum cascade lasers (QCLs). In both devices, the antenna structure consisted of two rectangular nano-rods with rounded ends, separated by a gap. At the resonances of the antennas, intense nanometric optical spots (~λ/20 for the near-ir plasmonic laser antenna and ~λ/70 for the mid-ir plasmonic laser antenna) were demonstrated in the antenna gap. However, there were also intense optical spots located at the two outer ends of the antenna structures [5-7]. The elimination of these side optical spots would produce a *single* subwavelength optical spot in the near field, which would be more suitable for spatially-resolved high-resolution chemical and biological applications [8-10]. In addition, it would be also very interesting to study, on a more basic level, the characteristics of the bowtie structure as compared with the nano-rod structure. In this letter, mid-ir bowtie plasmonic laser antennas are reported. The devices are demonstrated to provide spatial field confinement as small as 130 nm, and can sufficiently suppress the field enhancement at the outer ends of the antenna.

Our device is fabricated by defining a bowtie structure consisting of a pair of gold fan-like segments on the facet of a quantum cascade laser. The narrow ends of the segments are facing each other and are separated by a nanometric size gap. The antenna axis is orientated along the laser polarization. Antenna dipolar resonances are achieved when the length of each antenna segment approximately equals an odd integer number of half surface plasmon wavelengths [5, 7, 11-14]. In this situation, the field enhancement in the gap is maximized because the two narrow ends constituting the antenna gap have charges of opposite sign and the charges accumulated there are maximized. Physically a nano-capacitor is formed at the antenna gap, leading to an intense localized electric field. In the bowtie antenna, due to the large radius of curvature of the outer ends of the antenna segments, the charges concentrated there have a much lower density than at the narrow ends, leading to a substantially smaller field enhancement than in the gap. Therefore, in addition to producing a very intense localized optical spot in the antenna gap, the bowtie structure will provide a reasonably large ratio of the intensity of the optical spot in the antenna gap to that of the side spots at the outer ends of the antenna.

QCLs are semiconductor lasers based on optical transitions between quantum confined states in the conduction band [15, 16]. By tailoring the thickness of the quantum well layers constituting the laser active region, the emission wavelength of mid-ir QCLs can be adjusted continuously from about 3 µm to 24 µm, covering the entire mid-ir "fingerprint region" [17]. Mid-ir QCLs have recently achieved a high level of technological maturity: they can provide hundreds of milliwatts of output power under continuous wave operation at and above room temperature; they have been demonstrated to be highly reliable [18]. Sensitive and selective analyses on a large variety of gas- and liquid-phase specimens have been demonstrated by absorption spectroscopy using mid-ir QCLs [19, 20].

2. Simulations

The finite-difference time-domain (FDTD) method [21] is used to carry out a comparative study of the bowtie and the nano-rod antennas. Schematics of the simulated antenna structures are shown in Fig. 1(a), with their geometric parameters indicated. The antennas have the same gap width and QCL material is used as the substrate in the model. The excitation source consists of a mid-ir plane wave polarized along the antenna axis. The plane wave is launched from the inside of the laser material at normal incidence to the substrate. The refractive index of the laser medium is taken as 3.15, which is the weighted average of the refractive indices of the two constituents of the laser active region: InGaAs and AlInAs. This is a good approximation because the wavelength in the laser medium (about 2.2 µm at λ=7.0 µm) is much larger than the thickness of each individual quantum well layer in the active region. Adaptive meshing is used in all the FDTD simulations [21]: the area around the antenna gap has a grid size of 5 nm and other parts of the simulation region have a grid size of 20 nm. This helps to reduce the amount of calculations without sacrificing the resolution around the antenna gap.
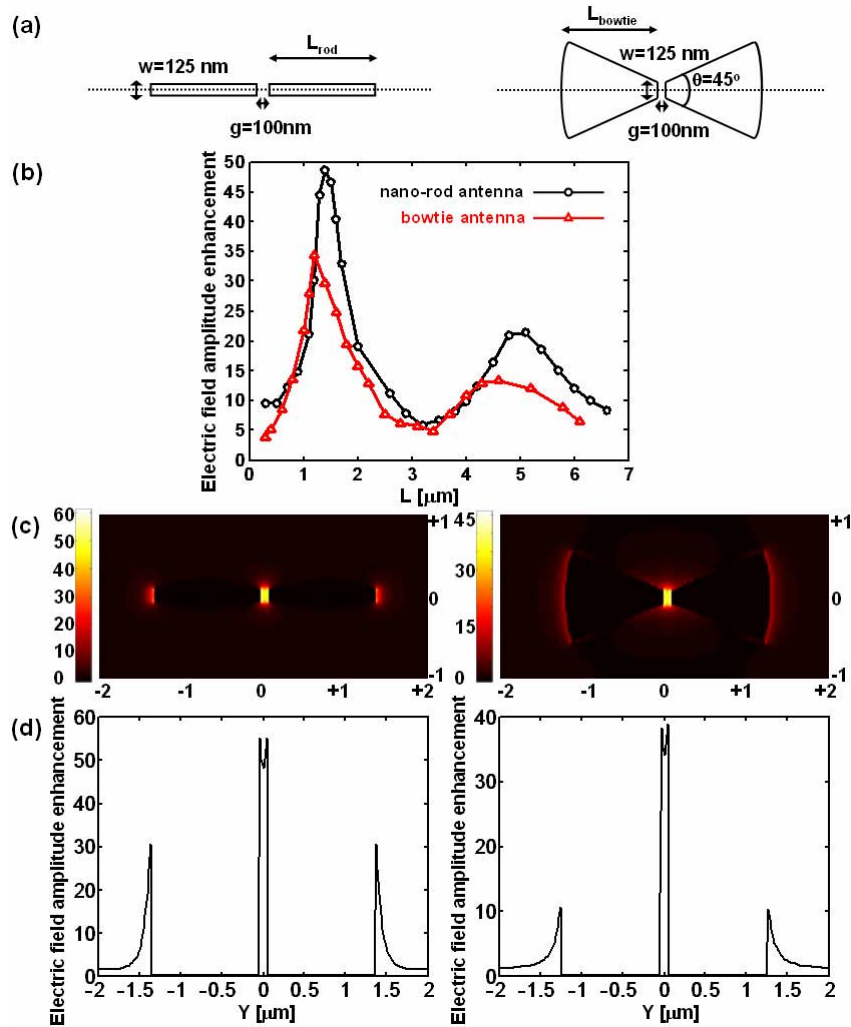
Fig. 1. A comparative study of the mid-infrared nano-rod antenna and the bowtie antenna by FDTD simulations. The free space wavelength of the incident plane wave normal to the plane is assumed to be 7 µm. (a) Simulated antenna structures. Left panel: a schematic of the nano-rod antenna. It is composed of two gold nano-rods separated by a nanometric gap. The size of the gap, the length and the width of the nano-rods, are indicated in the figure as g, L_{rod}, and w, respectively. Right panel: a schematic of the bowtie antenna. It consists of two gold fan-like segments separated by a nanometric gap. The geometries of the antenna are indicated in the figure. Both antennas have a thickness of 70 nm and they are defined on the output facets of quantum cascade lasers (QCLs). The facets are assumed to be coated with a 70 nm-thick electrically insulating layer of alumina. The antenna axes (dotted lines) are aligned with the polarization of the incident electric field. (b) Electric field amplitude enhancement vs. the antenna length L for the nano-rod antenna and the bowtie antenna. The field is calculated in the middle of the antenna gap at the level of the antenna top surface and is normalized to the amplitude of the incident field. The antenna length L is varied; other geometric parameters are kept unchanged and have the values as indicated in (a). (c) FDTD simulation results showing the electric field amplitude enhancement distribution of the two antennas at the first resonance (L_{rod}=1.4 µm and L_{bowtie}=1.2 µm). The enhancement is calculated on the plane that is at the same level as the antenna top surface. (d) Line scans of (c) along the antenna axes.

The field enhancement in the antenna gap is maximized when the antenna is illuminated at one of its resonant wavelengths. In Fig. 1(b), we present calculations of the electric field enhancement in the gap as a function of the length of each antenna segment (L_{rod} or L_{bowtie}),

allowing these resonances to be identified. In these simulations, the tip angle θ of the bowtie antenna is fixed at 45°. The width of the narrow ends w, the antenna gap g, and the antenna thickness are fixed at 125 nm, 100 nm, and 70 nm, respectively. The length of each antenna section L_{bowtie} is varied from 0.3 μm to 6.1 μm. Similarly, for the nano-rod antenna, the length of each rod L_{rod} is varied from 0.3 μm to 6.6 μm, with the other parameters kept unchanged. The two peaks at L_{bowtie}=1.2 μm and 4.6 μm for the bowtie antenna represent the first and the second dipolar antenna resonances, respectively; the corresponding resonance peaks for the nano-rod antenna occur at greater lengths: L_{rod}=1.4 μm and 5.1 μm. Antenna theory predicts that for a nano-rod antenna consisting of two highly conducting cylindrical rods with radius a, the antenna resonances appear at L_{res}=nλ/2 as a vanishes, where λ is the surface plasmon wavelength and n is an odd integer number [12,13]. If a is not infinitesimal, the resonances occur at $L<L_{res}$ and a general trend is that the resonances occur at smaller values of L if the shape of the antenna departs from the idealized case of a pair of infinitely thin rods [12, 13, 22]. Our simulation results of the nano-rod and the bowtie antennas are consistent with this trend. Moreover, Fig. 2(b) shows that the bowtie antenna has smaller maximum field amplitude enhancement compared with that of the nano-rod antenna. This is most likely due to a smaller Q factor for the former because of the larger antenna area, and correspondingly greater losses. This was also predicted by Crozier et al. for triangular optical antennas [11].

In Fig. 1(c), FDTD simulations of the 2D distributions of the field amplitude enhancement for the two antennas at the first resonance are presented. For both structures, the strong electric field is confined to the antenna gap with a spatial extent mostly determined by the gap size. Compared with the nano-rod structure, weaker field enhancement appears at the outer ends of the bowtie structure. This is more apparent in Fig. 1(d), in which line scans along the antenna axes of the data presented in Fig. 1(c) are given. Compared to the nanorod antenna, the bowtie antenna has a larger ratio of the near field amplitude in the gap to the near field amplitude at the antenna outer ends. The ratio is about 3.5 for the latter and about 1.8 for the former. This demonstrates the benefit of the bowtie structure, which is more efficient in suppressing the side spots. Simulations indicate that the suppression ratio is even larger for bowtie antennas with larger tip angles θ.

Note that the near field around the antenna structure is preferentially aligned with the antenna axis or the polarization of the incident field. The other field components are no larger than a few percent of this component. In all the simulations presented above, the antennas are gold. For modeling purpose, the gold was treated as a modified Debye material described by $\varepsilon(\omega)=\varepsilon_\infty+(\varepsilon_s-\varepsilon_\infty)/(1+i\omega\tau)+\sigma/(i\omega\varepsilon_0)$ with ε_s, ε_∞, ε_0, τ, and σ being the static relative permittivity, the relative permittivity at infinite frequency, the free space permittivity, the relaxation time, and the conductivity, respectively [23]. By using values ε_s=-15631, ε_∞=1, τ=1.08×10^{-14} sec, and σ=1.28×10^7 S·m^{-1}, we obtain a close match between $\varepsilon(\omega)$ and the experimentally obtained optical parameters in the wavelength range from 5 μm to 9 μm [24].

3. Experimental setup

A mid-ir a-NSOM (Fig. 2) based on a commercial atomic force microscope (AFM) (PSIA XE-120) is utilized to characterize the spatial profiles of the laser transverse modes [7,25] and the near field distribution of the bowtie antennas. The characterization of the transverse modes enables us to define the antennas at the laser mode maxima. For these measurements, we use commercial silicon AFM tips (Veeco Probes and Budget Sensors) that have resonance frequencies ranging from about 40 kHz to about 80 kHz. The tips are coated with 70 nm gold and the tip apex curvature is about 30 nm. The QCLs are driven by 125 ns current pulses with a repetition rate of about 500 kHz to reduce the average power, thereby preventing melting of the antennas and the metallic coatings of the AFM tips. In order to enhance the detection sensitivity, the interference between the near field scattered into the far field by the apex of the AFM tip and a reflected laser output is measured [25]. Therefore, the NSOM signal detected is

proportional to the near-field magnitude rather than the near-field intensity, assuming that the magnitude of the reflected laser field is a constant [26, 27]. A small metallic mirror is positioned with an appropriate angle near the AFM tip or close to the back output facet of the laser to create the reflected beam. The antennas are defined on the front facet of the QCLs. Two zinc selenide (ZnSe) lenses with numerical aperture of about 0.3 are used for collecting and focusing the mid-ir radiation onto a liquid-nitrogen-cooled mercury-cadmium-telluride (MCT) detector. The signal detected is demodulated at the second harmonic of the tapping frequency of the AFM tips by a lock-in amplifier (SRS830, Stanford Research Systems). This enables discrimination between contributions from the scattered near field and the background light [26, 27]. The latter mainly originates from scattering of the laser output by the tip shaft or the AFM cantilever [26, 27].
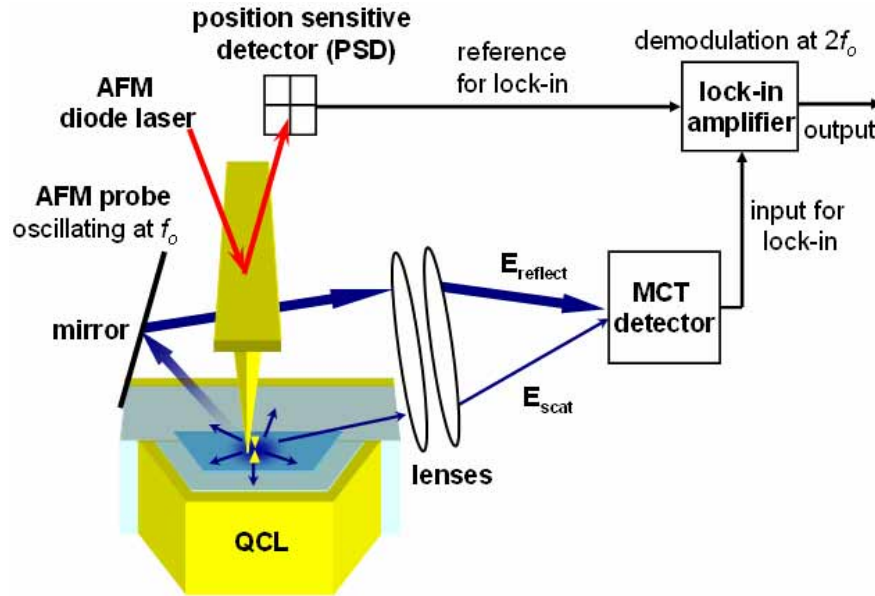

Fig. 2. A sketch of the apertureless mid-ir near-field scanning optical microscope used to characterize the laser transverse modes and the antenna near field on the facets of quantum cascade lasers (QCLs).

4. Bowtie antenna fabrications and NSOM experimental results

The devices on which the bowtie antennas are fabricated are buried heterostructure (BH) QCLs lasing at $\lambda \approx 7.0$ μm and with active region width of about 12 μm. The BH processing and the performance of these structures are described in Ref. [28]. Transverse mode imaging indicates that the QCLs that are employed lase in a TM_{00} mode with a single lasing spot at the center of the active region. After this initial mode characterization, the insulating alumina layer (70 nm) and the gold layer (70 nm) are deposited on the laser facet. The bowtie antennas are then defined by focused ion beam (FIB) milling where the laser mode has its maximum. Figure 3 shows the scanning electron microscope (SEM) images of one of the antennas fabricated. Our FDTD simulations [Fig. 1(b)] predict that it is resonant at $\lambda=7.0$ μm. The width of the antenna gap is about 94 nm. The four markers at the corners of the active region in Fig. 3(a) are defined by FIB milling before depositing the alumina and the gold layers. They are helpful for alignment of the antenna to the center of the laser active region.
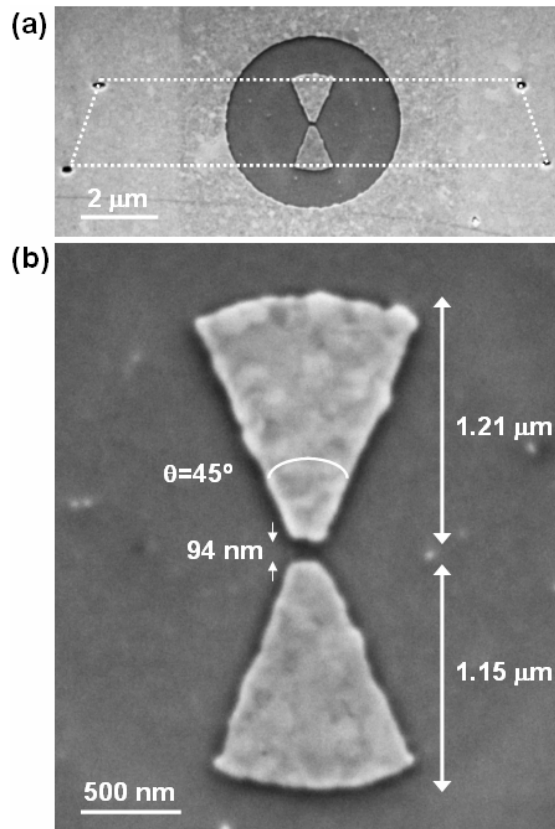
Fig. 3. Bowtie antenna fabricated by focused ion beam milling. (a) A scanning electron microscope (SEM) image of the antenna defined on the facet of a λ=7.0 µm quantum cascade laser (QCL). The dotted lines indicate the boundary of the cross section of the laser active region. The darker area is the milled region, in which the underlining alumina layer has been exposed. The lighter area is gold. (b) A zoom-in view of the antenna shown in (a).

In Fig. 4(a), the NSOM image and the AFM topography taken simultaneously are presented for the bowtie antenna shown in Fig. 3. From the NSOM image, it can be seen that the antenna generates a subwavelength spot in the antenna gap with strength considerably stronger than that of the side spots at the outer ends of the antenna. The line scan of the NSOM image along the antenna axis [Fig. 4(b)] shows that the center optical spot has a full-width at half-maximum (FWHM) of about 250 nm. The size is larger than the dimensions of the antenna gap, which is about 100 nm. This might be due to the finite radius of curvature of the AFM tip apex. One of the side peaks in the line scan has a height that is about 30% of that of the center peak, while the other side peak is about 10% of the center peak. The asymmetric side peaks might be due to the asymmetry of the antenna structure (Fig. 3), or might be due to the slightly different magnitude of the reflected signal (E_{ref} in Fig. 2) that occurs when the tip scans each outer end of the antenna. In recent work on nano-rod antennas, we demonstrated experimentally a resonant nano-rod antenna at λ=7.0 µm with a comparable gap size as the bowtie structure presented here [7]. The ratio of the center peak to the side peaks in the line scan of the NSOM image was about 2 [7]. By contrast, this ratio is between a factor of 3 to 10 for the bowtie antenna presented here, demonstrating that the bowtie structure suppresses the side spots more efficiently. A 3D view of the NSOM image [left panel of Fig. 4(a)] is shown in Fig. 4(c), which exhibits an intense center spot with a spot size of about 250 nm×200 nm. The large ratio between the center spot and the side spots is evident.
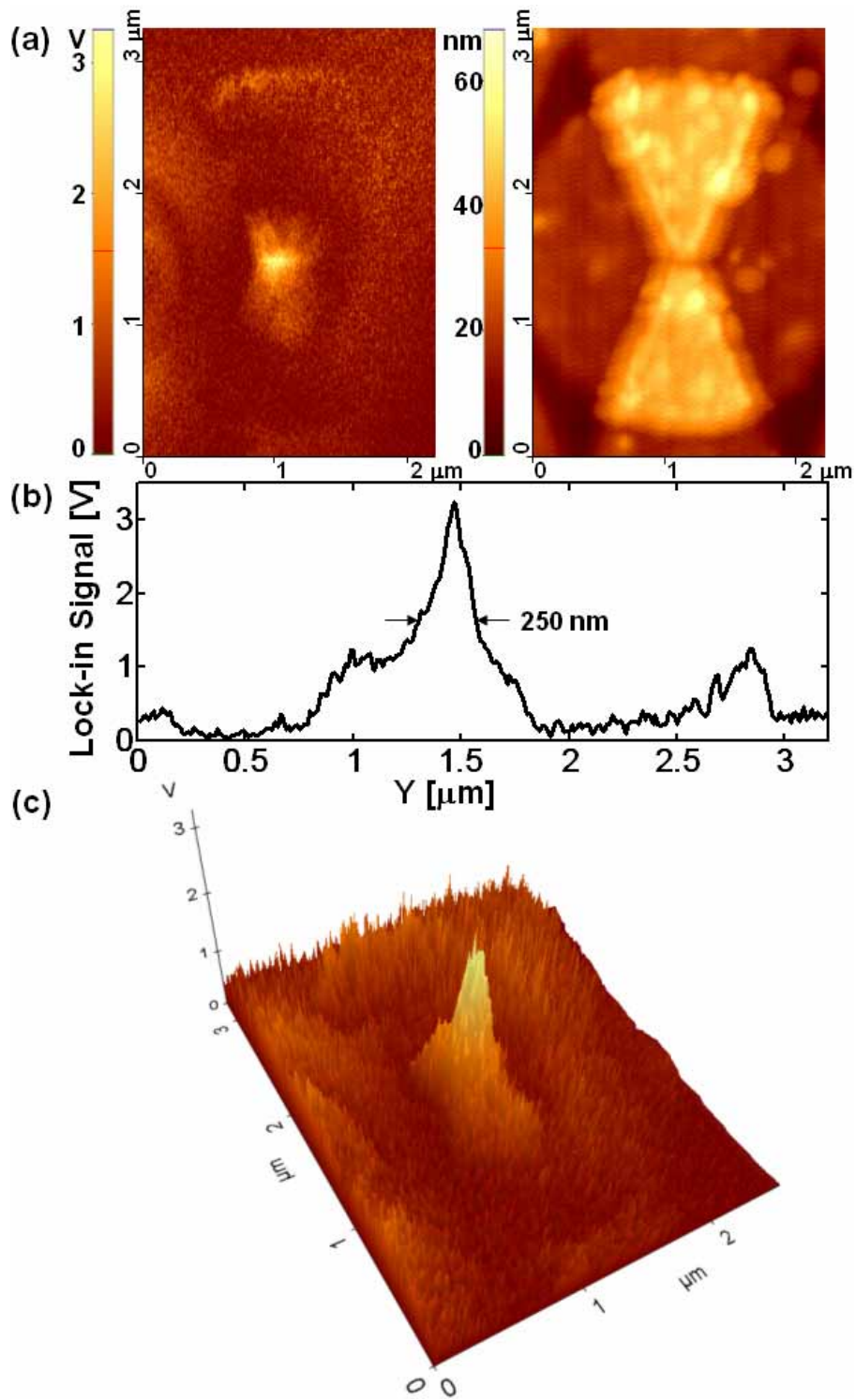
Fig. 4. Mid-ir apertureless-NSOM imaging of the bowtie plasmonic laser antenna. (a) NSOM image (left) and AFM topography (right) for the antenna shown in Fig. 3. The antenna is designed to be working at the first dipolar resonance with λ=7.0 µm. (b) Line scan of the NSOM image in (a) along the antenna axis. (c) A 3D view of the NSOM image in (a).

The electric field in the gap of the bowtie antenna can be estimated by considering the field strength in the QCL mode and the simulated field amplitude enhancement. The QCL used has an average output power of about 0.5 mW. The repetition rate of the current pulses was 500 kHz and the pulse width was 125 ns. The peak optical intensity of the laser mode is therefore about $2\times10^5 W/cm^2$. The optical intensity in the center of the antenna gap is therefore about $2.5\times10^8 W/cm^2$, corresponding to an electric field of about $2\times10^5 V/cm$.
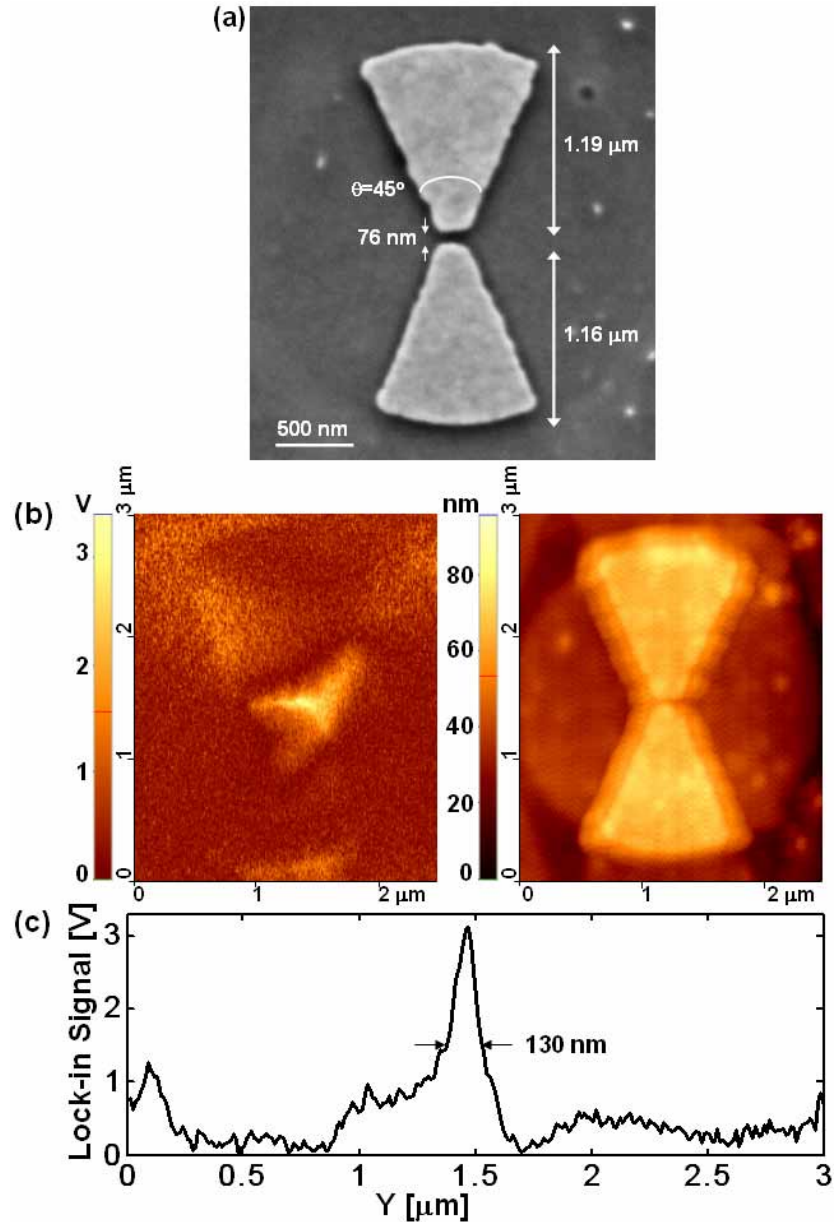

Fig. 5. Characterizations of another bowtie plasmonic laser antenna. (a) A scanning electron microscope image of the antenna. It has a smaller gap size compared with the antenna shown in Figs. 3 and 4. (b) Simultaneous NSOM image and AFM topography for the antenna. It is designed to be working at the first dipolar resonance with λ=7.0 μm. (c) Line scan of the NSOM image along the antenna axis. The center peak has a full-width at half-maximum of about 130 nm.

In Fig. 5(a), the SEM image of another bowtie antenna working at the first dipolar resonance is presented. The antenna gap width is about 76 nm, which is smaller than that of the bowtie antenna presented in Fig. 3. Figure 5(b) shows the NSOM image and the AFM topography taken simultaneously for this device. The line scan through its axis [Fig. 5(c)] shows correspondingly a smaller FWHM of about 130 nm. The optical spot in the center of the antenna gap is triangular with field enhancement close to the gap on the right slanting edges of the bowtie structure. This is most likely due to the fact that the antenna is defined slightly to the left of the laser mode maximum (the misalignment is about 0.6 μm, determined by measuring the distance between the location of the antenna and the center of the active region). The center-spot-to-side-spot ratio for this antenna is found to be larger than 3, in good agreement with the other device.

It should be pointed out that the near-field scattering efficiency of the AFM tip is different when the field is polarized parallel or perpendicular to the axis of the AFM tip: the former has a much higher efficiency [27]. Although the near field is primarily polarized perpendicular to the AFM tip in our experimental configuration, there is still a non-zero field component along the tip axis due to the pyramidal shape of the tip and the tilting of the tip axis in the experimental setup: all of these complicate a quantitative analysis.

5. Conclusions

We have demonstrated experimentally the bowtie plasmonic QCL antennas. The devices can provide confinement of the electric field in the antenna gap to dimensions of $\lambda/50 \sim \lambda/30$ at mid-ir wavelengths. Importantly, these devices efficiently suppress the field enhancement at the outer ends of the antenna structures. The center-spot-to-side-spot is about 3 to 10 for the bowtie structure, compared to a ratio of about 2 for the nano-rod structure. The peak intensity in the gap of the resonant bowtie antenna is estimated to be on the order of $0.1 GW/cm^2$. These compact active devices may find applications in high-resolution chemical and biological imaging and spectroscopy.